Emergent Materials (2020) 3:331–337
https://doi.org/10.1007/s42247-020-00103-3

ORIGINAL ARTICLE

PEG-assisted hydrothermal synthesis of porous $Li_3V_2(PO_4)_3$ frameworks for lithium-ion batteries

Yi Zhang[1] · Congchong Lingfei[1] · Renyuan Zhang[1]

Received: 7 January 2020 / Accepted: 22 April 2020 / Published online: 19 May 2020

Abstract

Porous $Li_3V_2(PO_4)_3$ frameworks have been synthesized via a simple hydrothermal route along with subsequent calcination. Polyethylene glycol (PEG-400) is employed as a soft template to control the morphology of the products. The porous frameworks consist of abundant $Li_3V_2(PO_4)_3$ nanowires which cross with each other to form a 3D network structure. Benefiting from the intriguing hierarchical structure, the unique $Li_3V_2(PO_4)_3$ electrodes exhibit excellent rate capability and good cyclability (96% of the initial discharge capacity retained after 500 cycles) in a voltage range of 3.0–4.3 V.

Keywords $Li_3V_2(PO_4)_3$ · Porous framework · PEG · Nanowire · Lithium-ion batteries

1 Introduction

Rechargeable lithium-ion batteries (LIBs) have played a significant role for applications in small electronic devices and electric vehicles owing to their ultra-long cycle life, low self-discharge, high power capability, and energy efficiency [1]. Cathode materials, such as $LiCoO_2$ [2, 3], $LiMn_2O_4$ [4, 5], and $LiNi_{1/3}Co_{1/3}Mn_{1/3}O_2$ [6, 7], have been successfully brought into the market. Besides, the lithium transition-metal phosphates such as $LiMPO_4$ (M = Fe, Mn, Co, Ni) [8–17] and $Li_3V_2(PO_4)_3$ [18–22] have also attracted tremendous attention for their stable frameworks, relatively high potential plateaus, and large theoretical capacities. The monoclinic $Li_3V_2(PO_4)_3$ (LVP) exhibits high operating potential (3.0–4.8 V) and theoretical capacity (197 mAh g^{-1} with three lithium ions extracted completely). Due to the open three-dimensional (3D) Na superionic conductor (NASICON) framework, the LVP can offer a more thermodynamically stable structure and rapid lithium-ion diffusion channels in comparison with $LiFePO_4$ [23]. However, like other lithium transition-metal phosphates, the commercialization of LVP is hindered by two main obstacles: the inherent low electronic conductivity (2.4×10^{-7} S cm^{-1} at room temperature) and low Li^+ diffusion coefficient because of the large particle size [22]. These two defects adversely decrease the electric capacity and rate capability.

Functional nanostructured materials usually have a short Li^+ insertion/extraction distance, large contact area, and facile strain relaxation when they serve as electrode materials, so tailoring the dimension of materials into nanoscale can effectively improve the rate capability [24]. However, the high surface energy of nanomaterials always causes serious self-aggregation, reducing the effective contact areas between active materials and electrolytes. Porous frameworks can offer a large surface area, cut down the Li^+ transport distance and overcome the agglomeration phenomenon, which can thus enhance the rate performance and cycling stability [25–31].

In this work, we present a simple hydrothermal method to fabricate porous LVP frameworks by using polyethylene glycol (PEG-400) as a soft template. The porous frameworks consist of abundant LVP nanowires which cross with each other to form a 3D network structure. As cathode materials, the porous LVP frameworks with specifically hierarchical morphology exhibit satisfactory rate capability (127 mAh g^{-1} at 0.1 C and 70 mAh g^{-1} when up to 5 C) and cycling stability (96% of the initial discharge capacity

Yi Zhang and Congchong Lingfei contributed equally to this work.

Electronic supplementary material The online version of this article (https://doi.org/10.1007/s42247-020-00103-3) contains supplementary material, which is available to authorized users.

✉ Renyuan Zhang
ryzhang@tongji.edu.cn

[1] Institute of New Energy for Vehicles, Shanghai Key Laboratory for Development and Application of Metallic Functional Materials, School of Materials Science and Engineering, Tongji University, Shanghai 201804, People's Republic of China

retained after 500 cycles), suggesting their promising applications in LIBs.

2 Experimental

2.1 Synthesis of porous LVP frameworks

All the chemicals are of analytical grade and used without further purification. The porous LVP frameworks (LVP-PF) are prepared by a convenient hydrothermal process along with subsequent calcination. In a typical procedure, 3 mmol LiAc, 2 mmol NH_4VO_3, 3 mmol $NH_4H_2PO_4$, and 4 mmol oxalic acid are dissolved in a mixture of 50 mL deionized water and 5 mL PEG-400 under magnetic stirring to form a clear lawn green solution after 8 h at room temperature. Then, the precursor solution is transferred into a Teflon-lined autoclave and heated to 180 °C for 48 h. After cooling to the room temperature, a cylindrical blue transparent hydrogel is obtained. This hydrogel is heated at 120 °C in a vacuum drying oven for 12 h to form green powders. These powders are first sintered at 350 °C for 2 h then calcined at 750 °C for 2 h under N_2 with a heating rate of 5 °C min^{-1} to obtain the porous LVP frameworks. In addition, LVP-comparison (LVP-C) samples are also prepared without PEG-400 under the same conditions.

2.2 Material characterization

The morphology and microstructure of the products were investigated using field-emission scanning electron microscopy (FESEM, LEO 1430VP, Germany) and high-resolution transmission electron microscopy (HRTEM, JEOL JEM-2010). The crystal structures of the samples were collected by X-ray diffraction (XRD) (Bruker D8 advance) with Cu Kα radiation. The angular resolution in 2θ scans was 0.4° over a 2θ range of 10–60°.

2.3 Electrochemical measurements

The electrochemical characterization was carried out in two-electrode electrochemical cells. The tap density of the LVP nanowire frameworks is about 0.68 g cm^{-3}. The electrodes were prepared by milling a mixture of 80 wt% active materials, 10 wt% acetylene black, and 10 wt% poly (vinyl difluoride) (PVDF) in N-methylpyrrolidinone (NMP) to form a homogeneous slurry. The slurry of the mixture was pasted uniformly on an aluminum foil current collector, and the electrode was then dried under vacuum at 110 °C for 12 h. Test cells were assembled in an argon-filled glovebox using Li foil as both the counter and reference electrodes, and polypropylene (PP) film as the separator. The electrolyte was 1 M $LiPF_6$ in a mixture of ethylene carbonate (EC) and dimethyl carbonate (DMC) (1:1 v/v). Galvanostatic charge/discharge tests of the assembled cells were performed in the potential range of 3.0–4.3 V under various current densities. The C-rates used were based on the theoretical capacity 133 mAh g^{-1}. Cyclic voltammetry (CV) studies were carried out on an electrochemical workstation (CHI660 C) between 3.0 and 4.3 V at a scan rate of 0.1 mV s^{-1}.

3 Results and discussion

The preparation of LVP-PF is based on a hydrothermal method, which is schematically illustrated in Fig. S1. A blue transparent hydrogel precursor is obtained after the hydrothermal process (Fig. S2). After drying the blue hydrogel at 120 °C, green powders are obtained and speculated to be $Li_xVOPO_4 \cdot yH_2O$ according to the X-ray diffraction (XRD) results (Fig. S3) [32]. The LVP samples are well crystallized after further calcination at 750 °C. The XRD patterns present sharp diffraction peaks (Fig. 1a), which can be indexed to the monoclinic LVP phase with a space group of $P2_1/n$ [33]. No other secondary phase is detected, indicating the high phase purity of the samples. The refined XRD pattern of the LVP-PF sample and the corresponding crystallographic data are shown in Fig. S4 and Table S1. XPS analysis of the V 2p in LVP-PF is shown in Fig. S5.

The monoclinic LVP has a NASICON three-dimensional framework structure and Li-ion can easily diffuse through the well-defined ion channels. As illustrated in Fig. 1b, the VO_6 octahedrons share all their corners with PO_4 tetrahedrons and vice versa, forming monoclinic $P2_1/n$ space groups. The basic $[V_2(PO_4)_3]^{3-}$ unit consists of two VO_6 octahedrons and three PO_4 tetrahedrons and each $[V_2(PO_4)_3]^{3-}$ unit is connected to six other units, so the interstitial space is large enough to hold three Li ions per structure formula [34–39]. The three distinct lithium sites consist of Li1 site, one tetrahedral site, and two pseudo-tetrahedral sites (Li2 and Li3) [34]. During the electrochemical cycling, Li3 is removed first to form the $Li_2V_2(PO_4)_3$ structure. However, there are two possible structures for $Li_1V_2(PO_4)_3$: during the electrochemical extraction process, the Li ions are occupied only at the Li2 sites, which means the Li1 is removed ahead of Li2; during the reinsertion process, both Li1 and Li2 sites are partially occupied by Li ions in $Li_1V_2(PO_4)_3$ structure [35, 39].

The PEG-400 soft template plays an important role in the formation of the LVP hierarchical structure. When PEG-400 is introduced into the hydrothermal reaction system, the morphology of LVP-PF powdered precursor contains numerous nanowires before calcination (Fig. S4a). After calcination at 750 °C for 2 h under N_2, the LVP-PF forms a porous framework structure which consists of abundant nanowires (Fig. 2a–c). These nanowires cross with each other to form a 3D network structure with plenty of pores inside, which can provide continuous electron transport pathways. The pore

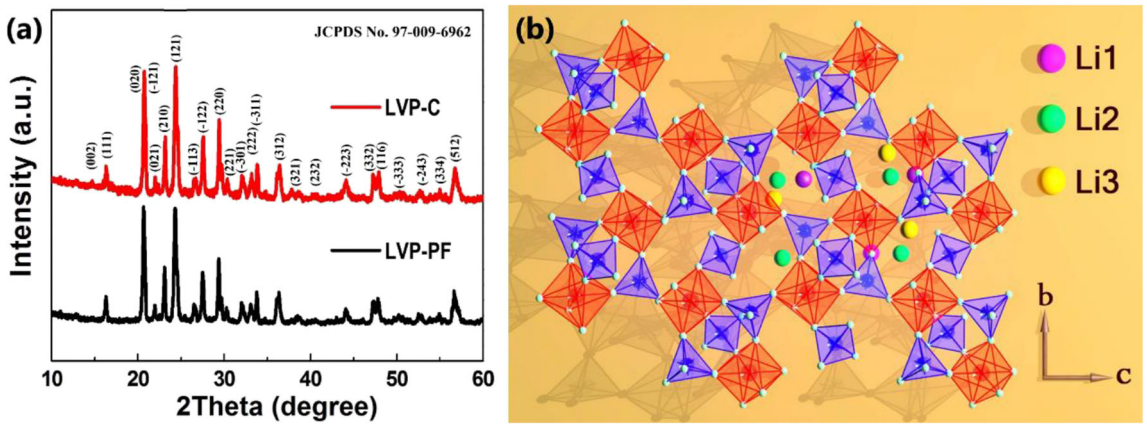

Fig. 1 **a** XRD patterns of the LVP-PF and LVP-C. **b** Schematic illustration of the monoclinic LVP framework

diameters are in the range of 50–250 nm and the diameters of nanowires are in the range of 40–70 nm, which can not only enhance the effective contact areas between active materials and electrolytes, but also facilitate the ion diffusion kinetics. However, in contrast to LVP-PF hierarchical structure, without PEG-400 assistance, the LVP-C shows irregular

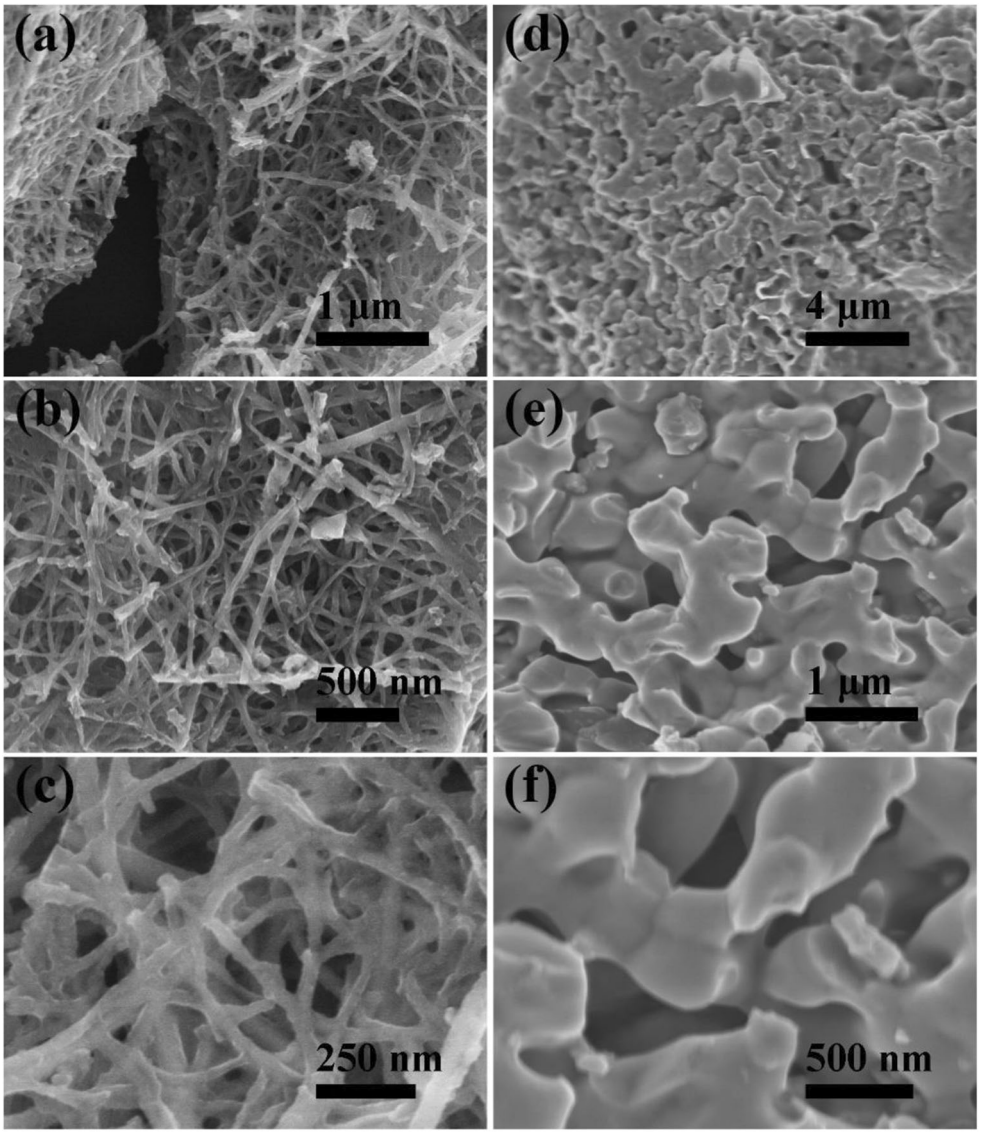

Fig. 2 SEM images of the LVP-PF (**a**, **b**, **c**) and LVP-C (**d**, **e**, **f**)

morphology since the LVP particles are severely agglomerated after the calcination process (Fig. 2d–f). These bulky structures have fewer effective contact areas because the electrolytes contact merely the outer surfaces of LVP particles.

The porous framework and intercrossed nanowire structure of the LVP-PF sample can also be clearly observed in TEM images (Fig. 3a–c). The diameters of nanowires are in the range of 40–70 nm, which coincides with that from the SEM images. The formation of large contact areas and continuous electron transport pathways can enhance the electrochemical performance. Furthermore, Fig. 3d presents a lattice fringe with *d*-spacing of 0.33 nm (inset), corresponding to the $\overline{1}$ 22 plane of monoclinic LVP. Besides, an amorphous carbon layer with about 2 nm thickness is observed on the surface of the LVP nanowire, which may come from the decomposition of PEG-400 during high-temperature calcination under N_2 atmosphere. The conductive carbon layer can increase the inherent low electronic conductivity of LVP.

In order to identify that the porous framework is in favor of the electrochemical performance, the coin-type cell is employed to evaluate the electrochemical behaviors of LVP-PF and LVP-C. Two Li^+ per formula unit are extracted/inserted in the potential range of 3.0–4.3 V. Figure 4a shows the cyclic voltammetry (CV) at a scanning rate of 0.1 mV s^{-1}. Both of the two samples present three couples of oxidation/reduction peaks between 3.0 and 4.3 V, corresponding to the relative extraction/insertion of Li^+. The CV of LVP-PF exhibits more highly symmetrical and obvious splitting redox peaks than that of LVP-C. The higher peak intensities and lower potential differences of LVP-PF indicate a better electrochemical reversibility and faster kinetics of the electrochemical reaction due to the specific porous framework structure.

Both of the LVP-PF and LVP-C electrodes present three couples of charge/discharge plateaus in Fig. 4b, demonstrating a two-phase transition during the electrochemical reactions. The two charge plateaus around 3.6 and 3.7 V correspond to the extraction of the first Li^+ in two steps due to the presence of an ordered $Li_{2.5}V_2(PO_4)_3$ phase while the second Li^+ is extracted through a single step around 4.1 V to form $LiV_2(PO_4)_3$ phase [35, 39]. These three corresponding discharge plateaus are attributed to reversible reinsertion of two Li^+ ions into the host lattices, which are associated with the V^{3+}/V^{4+} redox couple.

Rate and cycling performances are tested and the results are presented in Fig. 4c, d. The LVP-PF electrode has a capacity of 127 mAh g^{-1} at 0.1 C and remains 70 mAh g^{-1} when up to 5 C, implying the better rate capability than that of LVP-C electrode (about 50 mAh g^{-1} at 5 C). When the current density is turned back to 0.1 C, about 98% of the initial capacity is recovered for LVP-PF cathode, better than that of LVP-C cathode (about 93%). Then, both of the two electrodes are charged/discharged at 1 C to test the cycling ability. As shown in Fig. 4d, the capacity of LVP-PF has no obvious fading after 500 cycles (nearly 96% of the initial discharge capacity

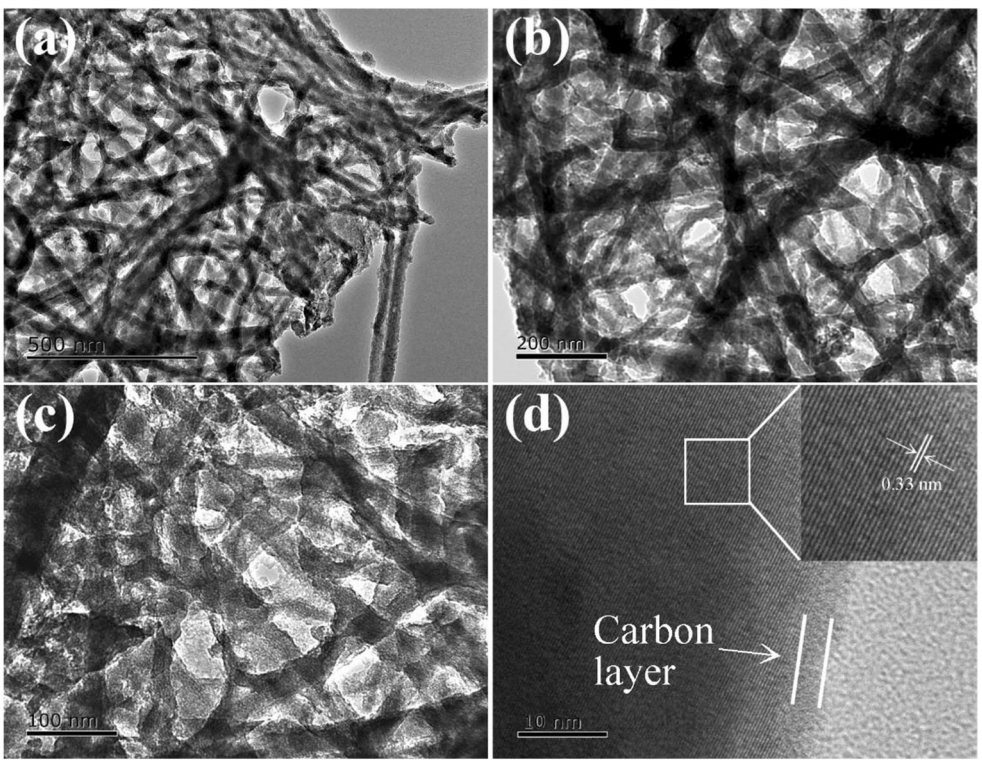

Fig. 3 TEM images of LVP-PF which show the porous framework and intercrossed nanowire structure (**a**–**c**). HRTEM image of LVP-PF (**d**): the inset shows a lattice fringe with *d*-spacing of 0.33 nm

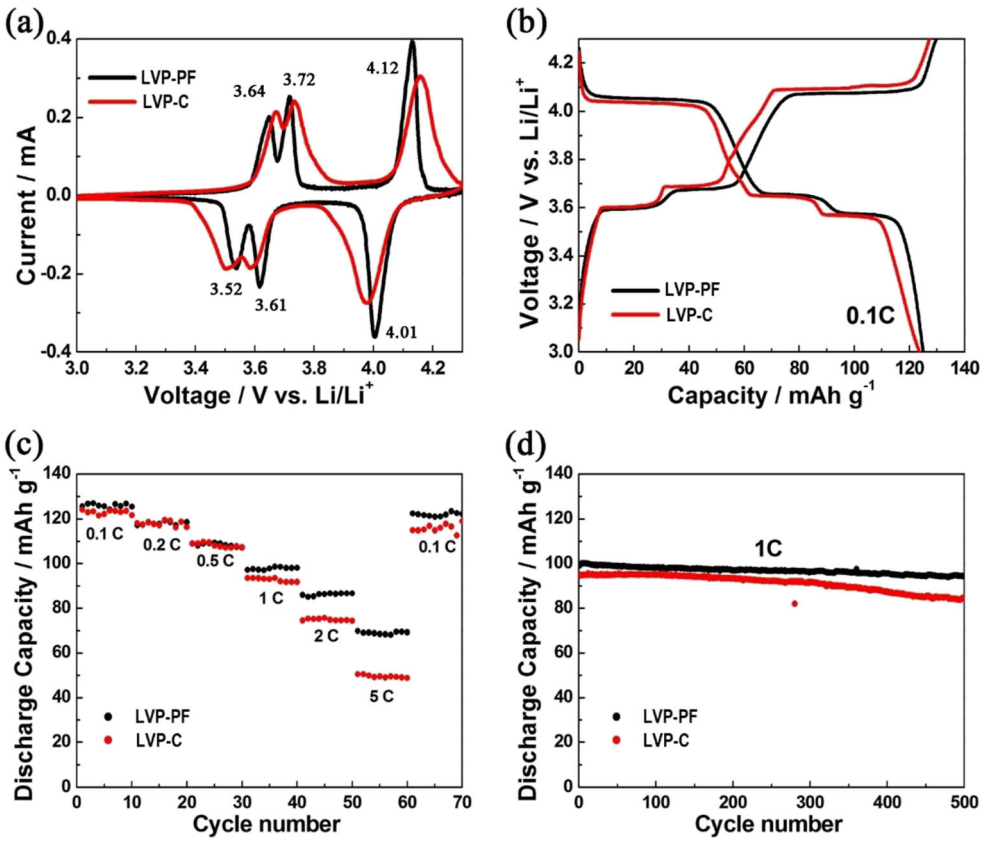

Fig. 4 The electrochemical properties of LVP-PF and LVP-C electrodes: (**a**) the CV curves of LVP-PF and LVP-C electrodes between 3.0 V and 4.3 V at a scan rate of 0.1 mV s^{-1}; (**b**) the charge/discharge curves of LVP-PF and LVP-C electrodes at various current rates; (**c**) rate capability at various current rates from 0.1 to 5 C; (**d**) cycle performance at a rate of 1 C

retained) while the LVP-C electrode shows an obvious decay after 300 cycles and only keeps about 85% of its initial discharge capacity. This excellent rate capacity and cycling ability of the LVP-PF could be attributed to the specific porous framework structure which provides a short distance for the Li-ion diffusion, a continuous electron transport pathway, and a large electrode–electrolyte contact area for high Li^+ ions flux across the interface. In addition, we compare our results with some recent related published works, which is listed in Table 1.

Table 1 Comparison of the electrochemical performance with recent published works

Material	Synthesis method	Mass loading (mg cm^{-2})	Current density (C)	Capacity (mAh g^{-1})	Cycles	Capacity retain	Ref.
LVP-PF	Hydrothermal method	3.0–3.5	1	127	500	96%	This work
LVP/C	Carbon-thermal reduction	3.1	1	125	50	99%	[40]
LVP/C	One-step pyro-synthesis	3.5	0.08	133	50	100%	[41]
$Li_2NaV_2(PO_4)_3$/C	Pyro-synthesis	4.5	0.4	92	300	100%	[42]
$Li_{2.99}K_{0.01}V_2(PO_4)_3$/C + N	Sol–gel process	2.2–2.5	1	159	100	78%	[43]
LVP/C	Carbon-thermal reduction	Non	0.1	119	50	98%	[44]
LVP/C	Wet-chemical coordination approach	Non	0.5	112	50	95.6%	[45]
$Li_3V_2(PO_4)_3$@MWCNTs@C	Sol-gel method	Non	5	123.5	300	96.3%	[46]
$Li_{2.4}Na_{0.6}V_2(PO_4)_3$@C	Sol–gel method	Non	1	121.6	200	95.6%	[47]
LVP/C	Carbon-thermal reduction	1.0–2.0	6	110	2000	94%	[48]
LVP@M-101	Carbon-thermal reduction	1.5–2.5	1	160	1000	70%	[49]
$Li_3V_2(PO_4)_3$-$Cu_{0.05}$/C	Self-catalyzed sol-gel approach	2.0–2.5	10	120	100	97%	[50]
LVP/C/N	Bio-template fabrication	Non	15	115	500	98%	[21]
$Li_3V_2(PO_4)_3$@C/AB	Spray drying method	2.5–3.0	1	119	200	98.5%	[51]

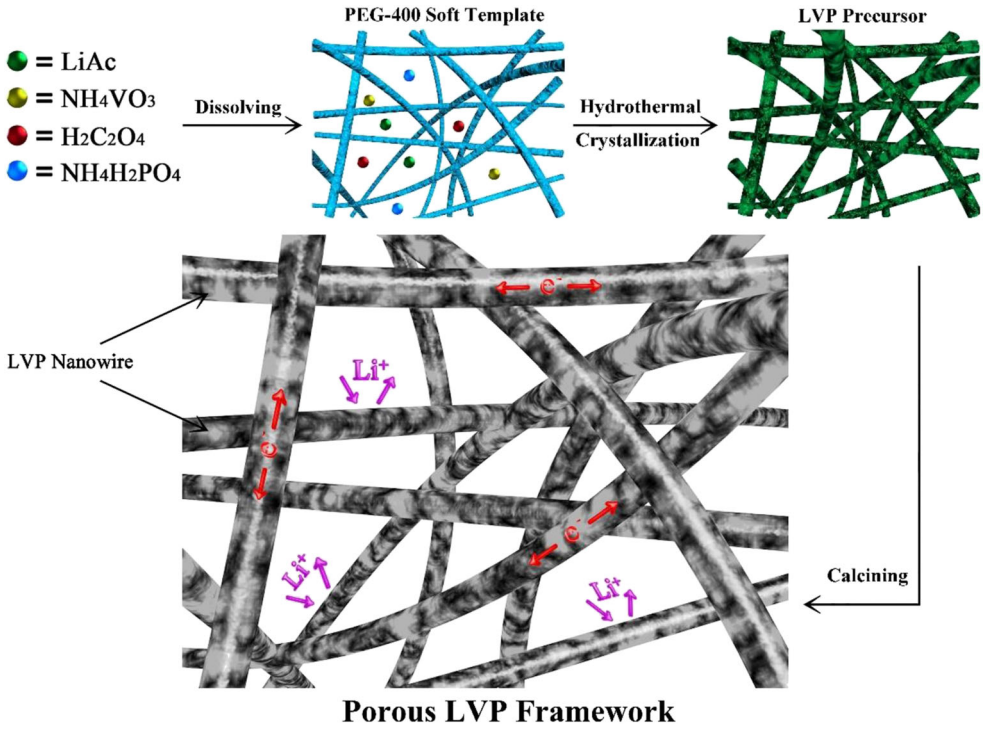

Fig. 5 Schematic diagram of the formation mechanism of LVP-PF

PEG nonionic surfactants usually act as structure-directing agents or soft templates to fabricate nanostructured materials with various morphology [52–54]. In this work, the existence of PEG-400 is essential in controlling the morphology of LVP. Based on the XRD, SEM, and TEM information, we conclude a mechanism as presented in Fig. 5. Firstly, PEG-400 is dissolved in deionized water to form long chains and each chain contains abundant active oxygen atoms. These active atoms produce strong interactions between metal ions and chains so that the nucleation and crystal growth of LVP are directed along these PEG chains. During the hydrothermal process, $Li_xVOPO_4{\cdot}yH_2O$ is crystallized with a nanowire shape. Due to these flexible PEG chains, the nanowires can easily cross with each other to form a 3D network structure. After the calcination treatment, this 3D network structure is retained with the crystallization of LVP and abundant pores are formed inside the frameworks. These porous frameworks can shorten the Li-ion diffusion distance and provide continuous electron transport pathways, so the electrochemical performance could be improved effectively.

4 Conclusions

In summary, we have successfully synthesized porous $Li_3V_2(PO_4)_3$ frameworks via a convenient hydrothermal process along with subsequent calcination by employing PEG-400 as a soft template. Such porous framework structure can provide not only the continuous electron transport pathways, but also a large electrode–electrolyte contact area and a short distance for the Li-ion diffusion. These advantages are in favor of the enhancement for the rate capability and cycling stability. It is therefore envisioned that this effective strategy can be generalized to fabricate other porous cathode materials for high performance energy storage applications.

Funding information We heartfully acknowledge the financial support from the National Natural Science Foundation of China (Grant Nos. 51602221), Shanghai Municipal Natural Science Foundation (16ZR1438400), and the Fundamental Research Funds for the Central Universities.

References

1. M. Li, J. Lu, Z. Chen, K. Amine, Adv. Mater. **30**, 1800561 (2018)
2. T. Wei, R. Zeng, Y. Sun, Y. Huang, K. Huang, Chem. Commun. **50**, 1962 (2014)
3. S. Kalluri, M. Yoon, M. Jo, et al., Adv. Energy Mater. **7**, 1601507 (2017)
4. H. Xia, Q. Xia, B. Lin, J. Zhu, J.K. Seo, Y.S. Meng, Nano Energy **22**, 475 (2016)
5. A. Tron, Y.D. Park, J. Mun, J. Power Sources **325**, 360 (2016)
6. M.S. Park, Phys. Chem. Chem. Phys. **16**, 16798 (2014)
7. C. Yang, X. Zhang, M. Huang, J. Huang, Z. Fang, ACS Appl. Mater. Interfaces **9**, 12408 (2017)
8. C.M. Julien, A. Mauger, Ionics **19**, 951 (2013)
9. M. Saubanere, E. McCalla, J.M. Tarascon, M.L. Doublet, Energy Environ. Sci. **9**, 984 (2016)
10. L.-H. Hu, F.-Y. Wu, C.-T. Lin, A.N. Khlobystov, L.-J. Li, Nat. Commun. **4**, 1687 (2013)

11. A. Eftekhari, J. Power Sources **343**, 395 (2017)
12. X. Wang, Z. Feng, J. Huang, et al., Carbon **127**, 149 (2018)
13. Y. Deng, C. Yang, K. Zou, X. Qin, Z. Zhao, G. Chen, Adv. Energy Mater. **7**, 1601958 (2017)
14. W. Zhang, Z. Shan, K. Zhu, S. Liu, X. Liu, J. Tian, Electrochim. Acta **153**, 385 (2015)
15. K.J. Kreder III, G. Assat, A. Manthiram, Chem. Mater. **27**, 5543 (2015)
16. Y. Liu, Z. Lu, C. Deng, et al., J. Mater. Chem. A **5**, 996 (2017)
17. S. Karthickprabhu, D. Vikraman, A. Kathalingam, K. Prasanna, H.-S. Kim, K. Karuppasamy, Mater. Lett. **237**, 224 (2019)
18. J. Su, X.-L. Wu, J.-S. Lee, J. Kim, Y.-G. Guo, J. Mater. Chem. A **1**, 2508 (2013)
19. W. Li, B. Song, A. Manthiram, Chem. Soc. Rev. **46**, 3006 (2017)
20. C. Liu, R. Masse, X. Nan, G. Cao, Energy Storage Mater. **4**, 15 (2016)
21. Y. Chen, K. Xiang, Y. Zhu, et al., J. Alloys Compd. **782**, 89 (2019)
22. H. Tan, L. Xu, H. Geng, X. Rui, C. Li, S. Huang, Small **14**, 1800567 (2018)
23. Y. Wang, P. He, H. Zhou, Energy Environ. Sci. **4**, 805 (2011)
24. L. Zhou, K. Zhang, Z. Hu, et al., Adv. Energy Mater. **8**, 1701415 (2018)
25. Q. Wei, F. Xiong, S. Tan, et al., Adv. Mater. **29**, 1602300 (2017)
26. L. Duan, X. Zhang, K. Yue, Y. Wu, J. Zhuang, W. Lu, Nanoscale Res. Lett. **12**, 109 (2017)
27. S. Wei, J. Yao, B. Shi, Solid State Ionics **305**, 36 (2017)
28. J. Song, H. Bin, C. Zhu, et al., J. Mater. Sci. Mater. Electron. **29**, 12216 (2018)
29. Q. Fan, Y. Zhang, Q. Xu, et al., Energy Storage Mater. **21**, 457 (2019)
30. X. Chen, P. Hu, J. Xiang, R. Zhang, Y. Huang, ACS Appl. Energy Mater. **2**, 5214 (2019)
31. R. Zhang, Y. Du, D. Li, et al., Adv. Mater. **26**, 6749 (2014)
32. H.-L. Huang, K.-H. Lii, S.-L. Wang, J. Chin. Chem. Soc. **61**, 199 (2014)
33. B. Pei, Z. Jiang, W. Zhang, Z. Yang, A. Manthiram, J. Power Sources **239**, 475 (2013)
34. S.C. Yin, H. Grondey, P. Strobel, M. Anne, L.F. Nazar, J. Am. Chem. Soc. **125**, 10402 (2003)
35. S. Lee, S.S. Park, J. Phys. Chem. C **116**, 25190 (2012)
36. H. Chen, Z.-K. Wang, G.-D. Li, et al., RSC Adv. **5**, 31410 (2015)
37. W. He, X. Zhang, X. Du, et al., Electrochim. Acta 112, 295. (2013)
38. L. Wang, J. Bai, P. Gao, X. Wang, J.P. Looney, F. Wang, Chem. Mater. **27**, 5712 (2015)
39. X. Rui, Q. Yan, M. Skyllas-Kazacos, T.M. Lim, J. Power Sources **258**, 19 (2014)
40. J. Yan, Y. Cao, F. Liu, RSC Adv. **6**, 113228 (2016)
41. S. Kim, J. Song, B. Sambandam, et al., Mater. Today Commun. **10**, 105 (2017)
42. M.H. Alfaruqi, S. Islam, J. Song, et al., Chem. Phys. Lett. **681**, 44 (2017)
43. C. Wang, Z. Li, H. Liu, Y. Wang, New J. Chem. **41**, 8772 (2017)
44. X. Cui, T. Liu, X. Zhang, X. Xiang, Ionics **23**, 3289 (2017)
45. Q. Ni, Y. Bai, Z. Yang, et al., J. Alloys Compd. **729**, 49 (2017)
46. L.-B. Zhang, L.-Z. Wang, J. Yan, Ionics **24**, 629 (2018)
47. M. Li, Z. Zuo, J. Deng, et al., J. Mater. Sci. **53**, 10327 (2018)
48. T. Chen, J. Zhou, G. Fang, et al., ACS Sustain. Chem. Eng. **6**, 7250 (2018)
49. Y. Liao, C. Li, X. Lou, et al., Electrochim. Acta **271**, 608 (2018)
50. J. Yan, H. Fang, X. Jia, L. Wang, J. Alloys Compd. **730**, 103 (2018)
51. Y. Li, J. Wang, Z. Zhou, et al., J. Alloys Compd. **774**, 879 (2019)
52. X. Gou, F. Cheng, Y. Shi, et al., J. Am. Chem. Soc. **128**, 7222 (2006)
53. Y.-X. Lu, Y. Jiang, Z. Yang, J.-T. Han, Y.-H. Huang, J. Ma, J. Alloys Compd. **559**, 203 (2013)
54. H. Shen, W. Xiang, X. Shi, B. Zhong, H. Liu, Ionics **22**, 193 (2016)